

Numerical investigation of hydrodynamic/acoustic splitting methods in finite volumes including rotating domains

Joscha PIEPIORKA⁽¹⁾ and Otto VON ESTORFF⁽¹⁾

⁽¹⁾Hamburg University of Technology, Institute of Modelling and Computation, Germany, Email: mub@tuhh.de

Abstract

In today's product development, the behavior of technical applications including rotating components (e.g., radial or axial fans) is increasingly important. Especially the noise emission is a major challenge to be handled by the manufacturers. Alongside expensive experimental investigations, reliable numerical simulations to predict the flow induced noise are gaining more and more importance. The paper will present first numerical results of an axial fan benchmark case. A simplified model of the experimental setup is used for a scaleadaptive CFD simulation. Based on incompressible CFD results, the acoustic quantities are modeled by a finite volume approach, which has been developed in the software framework OpenFOAM[®]. Different hydrodynamic/acoustic splitting methods are used to investigate the flow induced noise including the rotating domain of the fan. Special focus is placed on velocity terms and their influence onto aeroacoustic source and wave propagation effects. For this purpose, different hydrodynamic/acoustic splitting methods are analyzed and reformulated. The resulting sound fields are computed and interpreted based on the theoretical assumptions. Finally, the computational effort in the finite volume framework is discussed and the results are compared to experimental data.

Keywords: CAA, HAS, axial fan

1 INTRODUCTION

The numerical prediction of flow induced vortex sound in the low Mach number range including rotating domains demands high accuracy and efficiency. Using hybrid methods like the hydrodynamic/acoustic splitting (HAS) gives one possibility to apply Computational Aeroacoustics (CAA) in a two-step approach. Starting with an incompressible Computational Fluid Dynamics (CFD) simulation, the acoustics is defined as compressible perturbations. As there are various methods including different theoretical derivations and assumptions, the application of the most suitable method considering accuracy and efficiency is oftentimes case dependent.

In this paper an axial fan benchmark case by Zenger et al. [1] is investigated numerically, which includes the necessity to discretize and model a rotating domain. Motivated by the Mach number scaling laws from Moon [2], velocity terms and their influence onto aeroacoustic source and propagation effects is focused by the application of different HAS approaches. First, a short introduction to the benchmark case is given. In addition to three well established HAS approaches, a new modified wave equation formulation is introduced in the theory chapter. The numerical simulation setups summarizing the important simplifications are presented for CFD and CAA each. Based on the experimental data obtained from the benchmark [1], the numerical flow results are presented and discussed. Finally, the sound fields computed by different HAS approaches are compared and investigated. In this context, the newly introduced wave equation formulation shows consistent and promising results. Summarizing the main features of the investigations, a conclusion and an outlook are given.

2 AXIAL FAN BENCHMARK CASE

The low pressure axial fan benchmark case for aeroacoustics by Zenger et al. [1] is used for numerical investigations. It includes a variety of experimental data for the flow as well as for the induced acoustics and is designed to generate low Mach number vortex sound. The fan with 9 blades and a diameter of 495 mm is placed into a short duct, which connects the anechoic inlet chamber with the pressure outlet side including the

electric drive. The volumetric flow rate is tuned to $1.4 \text{ m}^3/\text{s}$ and the revolutions per minute $n = 1486 \text{ min}^{-1}$ lead to a blade passing frequency (BPF) of 225 Hz (for further details see [1]). First numerical investigations were successfully done by Junger et al. [3], who showed good agreement between their prediction and the experimental data. Therefore, some ideas and model assumptions in the present investigation are based on [3].

3 HYDRODYNAMIC/ACOUSTIC SPLITTING

The disparities of scales in CAA can be handled by separating the physical phenomena in hydrodynamics and acoustics. For this purpose the pressure p , the velocity \mathbf{u} and the density ρ are split via

$$p = p^{\text{ic}} + p^{\text{a}}, \quad \mathbf{u} = \mathbf{u}^{\text{ic}} + \mathbf{u}^{\text{a}}, \quad \rho = \rho_0 + \rho^{\text{a}}, \quad (1)$$

into an incompressible flow part \square^{ic} and a compressible acoustic part \square^{a} , which are modeled in two separate simulations using a one-way coupling from incompressible CFD to induced aeroacoustics.

3.1 Acoustic perturbation equations

The acoustic perturbation equations (APE) by Ewert and Schröder [4] are formulated for different flow conditions including various sound source mechanisms and coupling effects. Especially for low Mach number vortex sound, the second variant is preferable and termed APE-2. Combining the three original equations using the homentropic change of state $\rho^{\text{a}} = c_0^2 p^{\text{a}}$ with the constant speed of sound c_0 leads to [5]

$$\frac{\partial p^{\text{a}}}{\partial t} + \bar{\mathbf{u}}^{\text{ic}} \cdot \nabla p^{\text{a}} + \rho_0 c_0^2 \nabla \cdot \mathbf{u}^{\text{a}} = -\frac{\partial p^{\text{ic}}}{\partial t} - \bar{\mathbf{u}}^{\text{ic}} \cdot \nabla p^{\text{ic}}, \quad (2)$$

$$\rho_0 \frac{\partial \mathbf{u}^{\text{a}}}{\partial t} + \rho_0 \nabla (\bar{\mathbf{u}}^{\text{ic}} \cdot \mathbf{u}^{\text{a}}) + \nabla p^{\text{a}} = 0. \quad (3)$$

Eqs. (2) and (3) describe the formation and propagation of flow sound influenced by a time mean velocity field $\bar{\mathbf{u}}^{\text{ic}}$. The dominant source term is given by the time derivative of the incompressible pressure (see Eq. (2)).

3.2 Perturbed convective wave equation

Based on Eqs. (2) and (3), Hüppe derived the Perturbed Convective Wave Equation (PCWE) [5]. Introducing the scalar acoustic potential ψ^{a} defined via

$$\mathbf{u}^{\text{a}} = -\nabla \psi^{\text{a}}, \quad (4)$$

the PCWE reads [5]

$$\frac{D^2 \psi^{\text{a}}}{Dt^2} - c_0^2 \Delta \psi^{\text{a}} = -\frac{1}{\rho_0} \frac{Dp^{\text{ic}}}{Dt}, \quad (5)$$

where the substantial time derivative is given by

$$\frac{D}{Dt} = \frac{\partial}{\partial t} + \bar{\mathbf{u}}^{\text{ic}} \cdot \nabla. \quad (6)$$

Since no additional assumptions are introduced in the derivation, Eq. (5) describes the same aeroacoustic phenomena as the APE-2 including the identical aeroacoustic source term. Note that the APE-2 as well as the PCWE are very efficient as only the incompressible pressure has to be updated in time from CFD to CAA. The velocity vector $\bar{\mathbf{u}}^{\text{ic}}$ is constant in time. This, however, restricts the application to problem definitions, where the fluctuations of \mathbf{u}^{ic} have negligible influence on the acoustics.

3.3 Linearized perturbed compressible equations

Seo and Moon derived an HAS approach, starting from the compressible Navier Stokes equations including the energy equation and the ideal gas law, termed Perturbed Compressible Equations (PCE) [6]. More stable and restricted to pure acoustics, they linearized the PCE for low Mach number vortex sound and called it LPCE [7].

3.3.1 Original system of equations

Defined for aeroacoustics including the isentropic exponent γ , the LPCE read [7]

$$\frac{\partial \rho^a}{\partial t} + (\mathbf{u}^{ic} \cdot \nabla) \rho^a + \rho_0 (\nabla \cdot \mathbf{u}^a) = 0, \quad (7)$$

$$\frac{\partial \mathbf{u}^a}{\partial t} + \nabla (\mathbf{u}^a \cdot \mathbf{u}^{ic}) + \frac{1}{\rho_0} \nabla p^a = 0, \quad (8)$$

$$\frac{\partial p^a}{\partial t} + (\mathbf{u}^{ic} \cdot \nabla) p^a + \gamma p^{ic} (\nabla \cdot \mathbf{u}^a) + (\mathbf{u}^a \cdot \nabla) p^{ic} = -\frac{Dp^{ic}}{Dt}, \quad (9)$$

where the substantial time derivative is defined by

$$\frac{D}{Dt} = \frac{\partial}{\partial t} + \mathbf{u}^{ic} \cdot \nabla. \quad (10)$$

Comparing the APE-2 and PCWE with Eqs. (7) - (9), the main differences can be identified in the coupling of acoustics and the velocities from CFD. Furthermore, the instantaneous velocity \mathbf{u}^{ic} is introduced in the LPCE, which also changes the definition of the substantial time derivative in Eq. (10). This leads to additional effort in noise prediction but improves the physical modeling.

3.3.2 New modified wave equation formulation

Based on the idea of Hüppe [5], a new convective wave equation formulation in the form of [8] is introduced for the LPCE [7]. As Eqs. (7) - (9) explicitly exclude all non-acoustical modes, the introduction of the acoustic scalar potential is valid. Inserting the relation given in Eq. (4) into Eq. (8) and using the instantaneous velocity field from the CFD (see Eq. (10)), gives

$$p^a = \rho_0 \frac{\partial \psi^a}{\partial t} + \rho_0 (\mathbf{u}^{ic} \cdot \nabla) \psi^a \xrightarrow{\text{Eq.(10)}} p^a = \rho_0 \frac{D\psi^a}{Dt}. \quad (11)$$

As it can be seen from Eq. (11), p^a is given by the time derivative of ψ^a scaled by ρ_0 . To reformulate the density equation, Eq. (4) is introduced to Eq. (7) via

$$\frac{\partial \rho^a}{\partial t} + (\mathbf{u}^{ic} \cdot \nabla) \rho^a = \rho_0 \Delta \psi^a \xrightarrow{\text{Eq.(10)}} \frac{D\rho^a}{Dt} = \rho_0 \Delta \psi^a. \quad (12)$$

Equation (12) clearly shows the relation of ρ^a as time integral of the scaled laplacian of ψ^a . Finally, inserting the acoustic potential from Eq. (4), using the relation from Eq. (11) into Eq. (9), and introducing the substantial time derivative from Eq. (10) gives

$$\frac{D^2 \psi^a}{Dt^2} - \underbrace{\gamma \frac{p^{ic}}{\rho_0} \Delta \psi^a}_I - \underbrace{\frac{1}{\rho_0} (\nabla \psi^a \cdot \nabla) p^{ic}}_{II} = -\frac{1}{\rho_0} \frac{Dp^{ic}}{Dt}. \quad (13)$$

The wave equation formulation reduces the LPCE to a very compact scalar form. Influenced by the instantaneous flow field from the CFD, all source and propagation effects from the underlying LPCE are included and the sound pressure can be post processed from ψ^a . Optionally, the acoustic density can be included via an additional time integration. Comparing the PCWE from Eq. (5) with Eq. (13), term *I* is different in the formulations and term *II* is an additional coupling term from LPCE. More detailed, term *I* can be transformed via the ideal gas law into the speed of sound c depending on time t and space x (term $I = c^2(x, t)$). In summary, the main differences of the wave equations are caused by the velocity definitions and the coupling effects between flow and acoustics (see term *II*).

4 NUMERICAL SIMULATIONS

The numerical simulations are performed with the Finite Volume Method (FVM). Based on the open source environment OpenFOAM[®] (v1712), the standard CFD utilities are used for the flow simulation. The aeroacoustics is modeled by a solver, which is introduced in the same software framework [9].

4.1 Fluid dynamics

A scaleadaptive unsteady Reynolds averaged Navier Stokes (uRANS SAS) simulation is performed for a simplified model of the axial fan using a $k-\omega$ -SST SAS turbulence model. The mesh includes ≈ 12 mio. cells neglecting all parts beneath the axial fan, the duct and the chamber walls from the experiment. The near wall resolution is done in an adequate way for the geometry without special wall layer treatment. This yields to y^+ -values for the rotor and the inner duct of $y^+ \approx 5$. For the remaining walls adaptive wall functions are used. Both chambers are connected by the duct, which includes a rotating mesh domain surrounding the rotor of the fan (see Figure 1). To couple the rotating mesh domain with the static mesh domains of the chambers, a sliding mesh technique via an Arbitrary-Mesh-Interface (AMI) [10] is applied. The boundary conditions are set by a uniform inflow velocity at the inlet, no-slip conditions at the walls and typical outflow conditions at the outlet. All system parameters are based on the experimental data [1]. To yield statistical results, the simulation is initialized and tuned with 14 revolutions. The final evaluation and the data export for acoustics includes 3.2 revolutions of the fan and a time signal length of $T_{\text{sim}} = 0.13$ s.

4.2 Aeroacoustics

To predict the induced aeroacoustics, different HAS approaches and the CFD results are used. The acoustic model is shown in Figure 1 and the mesh is designed for frequencies up to 700 Hz discretized with at least 10 points per wavelength. The chambers are extended in size including numerical damping zones for acoustic free field conditions and the rotating domain of the fan is congruent with the CFD rotating domain part. This leads to an acoustic mesh with ≈ 4.5 mio. cells. Like in the CFD model, the interfaces and the interpolation between static and rotating domains are handled via AMI [10]. All source fields are interpolated with a cut cell volume weight approach in space and a seventh order spectrally optimized scheme in time [11]. The time integration is performed with a storage optimized low dispersion and dissipation Runge-Kutta scheme of fourth order (LDDRK-45). The solver is developed for applications including rotating domains [9] and was successfully verified and used in previous publications [12]. As a consequence of the simplified model, the anechoic behavior of the wall that separates the inlet and the outlet chamber is not included (see Figure 1).

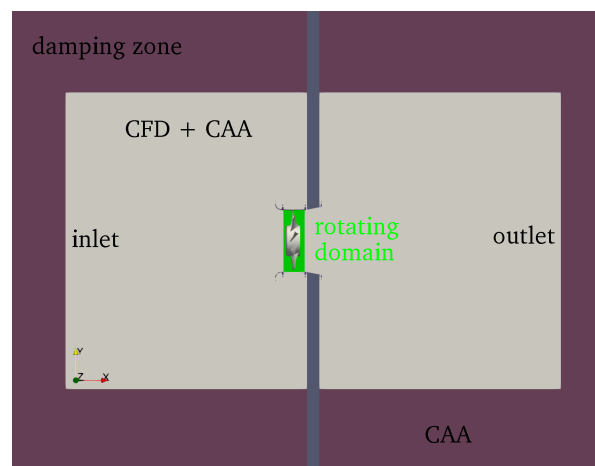


Figure 1. Schematic two dimensional sketch of the simplified CFD and CAA domains.

5 RESULTS

To discuss the complete numerical prediction of the fan aeroacoustics, the flow and the acoustic simulation results are presented separately in the following.

5.1 Flow results

The incompressible simulation of the turbulent flow leads to a static pressure difference between the chambers of $\Delta p_{\text{mean}}^{\text{ic}} = 123$ Pa, which is in accordance with the experimental data $\Delta p_{\text{mean}}^{\text{exp}} = 126.5$ Pa. As the angular velocity of the fan and the inflow velocity are fixed by the design parameters, no investigations are needed for them. Evaluating the axial mean velocity distributions in radial direction inside the duct gives a more detailed view (see Figure 2). On the suction side in Figure 2a, the SAS results show a good agreement with the experiment except for the near wall region of the duct ($r/r_{\text{duct}} > 0.95$). On the pressure side in Figure 2b, big differences between simulation and experiment are observable, which are caused by the geometric model simplifications. As only the fan without additional drive or shaft is present, no blockage effects can occur. Nevertheless, the main characteristics of the experiment are modeled by the SAS simulation. To detail the near wall regions, the wall pressure inside the duct is evaluated at four probe locations in Figure 3. The probe numbers in brackets refer to the numbering from [1]. The experimental reference for $T_{\text{exp}} = 30$ s is given in black and subsignal evaluation with $T_{\text{sim}} = 0.13$ s is plotted in gray for comparison to numerical SAS results, which are also given for T_{sim} each. All power spectral density (PSD) over frequency plots show the dominating influence of the blade passing effects. At first sight, the numerical results are in the same order of magnitude as the experimental measurements. Starting at probe 2 in the inlet region of the duct, the BPF at 225 Hz and its second harmonic are slightly over predicted in amplitude by the SAS. The general decay of the power is modeled with acceptable tolerance until frequencies $f \approx 1000$ Hz. However, investigating the first subharmonic peak shows a frequency shift and over prediction by the SAS. This behavior is strongly included in the solution of the SAS and also present at the outlet of the duct, where it is not expected from the experiment (see Figure 3d). As the subharmonic effects are known to be very important for the induced sound in this case [1], the influence is discussed in the following section. Evaluating the probes 7 and 8 in the tip gap region changing from suction to pressure side, shows the dominating periodicity effects of the passing blades. Despite the over estimation in Figure 3b, the global trend and the BPF orders are modeled by the SAS in a tolerable way.

In summary, the fluid flow generated by the axial fan can be approximated by the present SAS simulation. Despite the very coarse spatial discretization and the use of turbulence models, the main characteristics and qualitative effects can be predicted. However, the detailed estimation of the quantitative results shows the need for a more precise CFD model. As the CFD results are used for the computation of induced aeroacoustics, these facts are part of the final discussion.

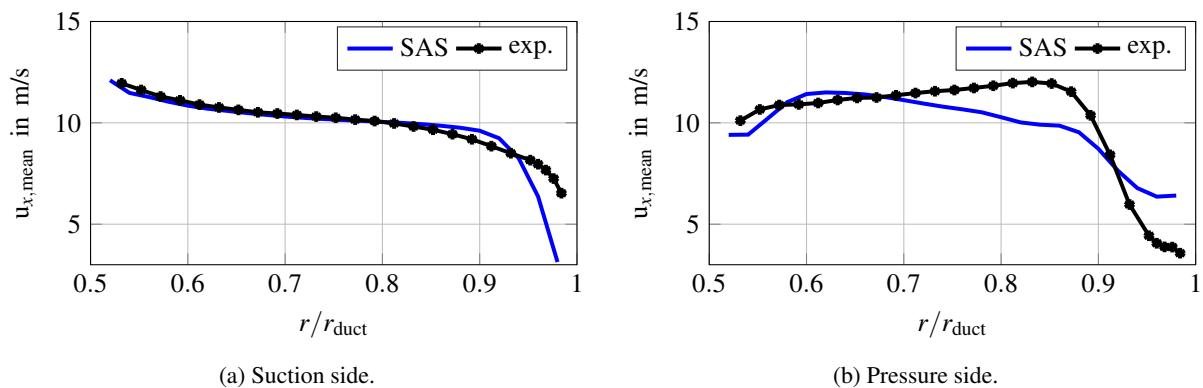


Figure 2. Time averaged velocity profiles inside the duct (radius of the duct $r_{\text{duct}} = 250$ mm).

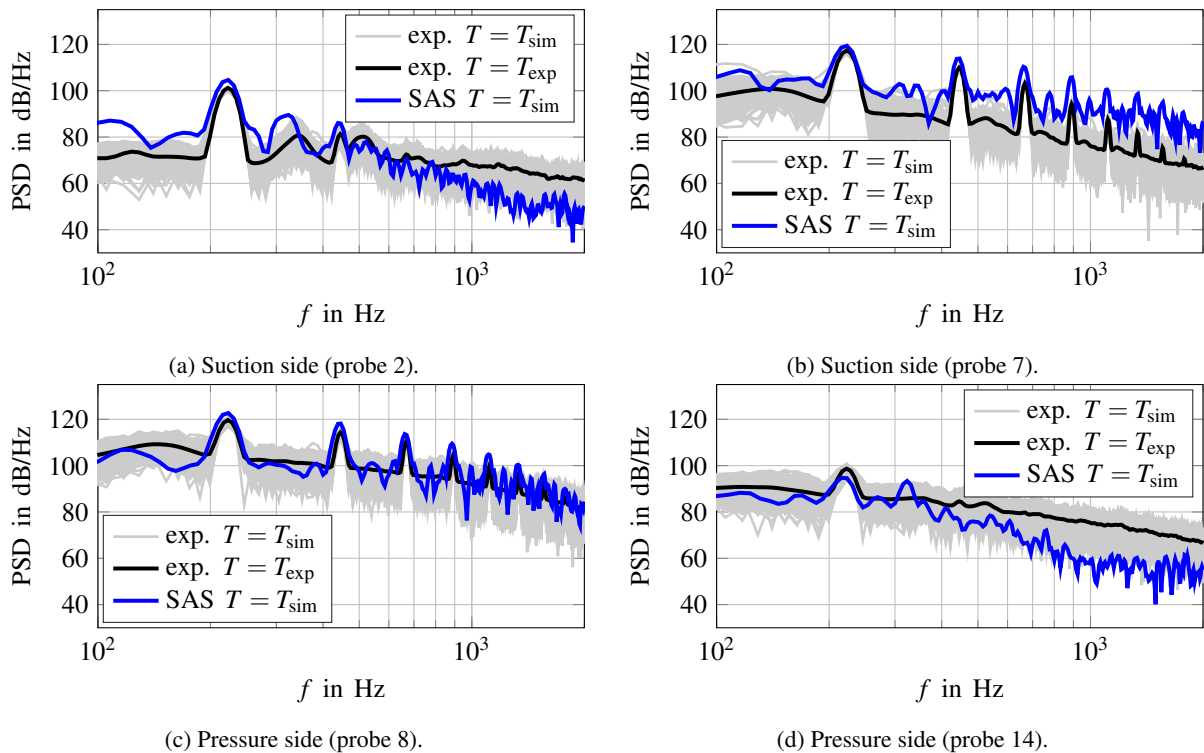
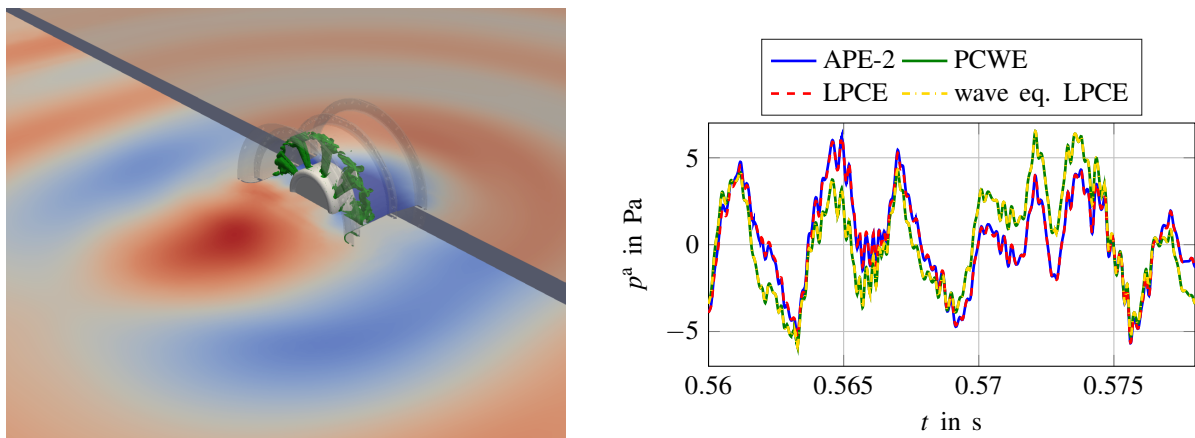


Figure 3. Wall pressure probes inside the duct.

5.2 Acoustic results

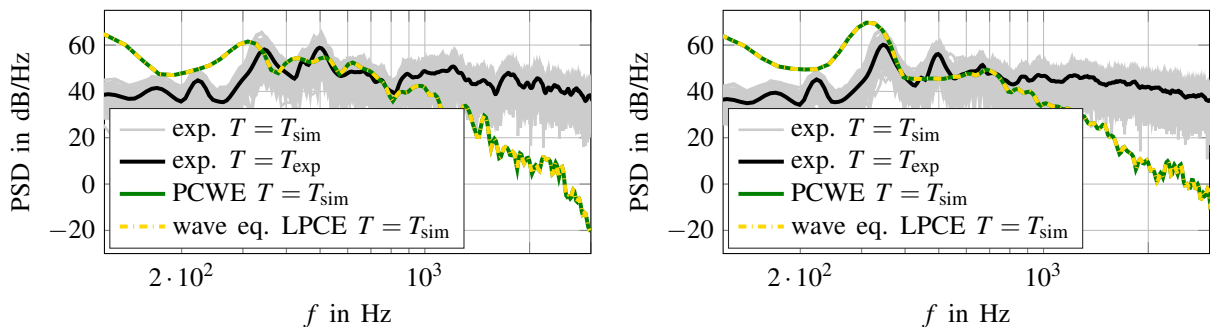
The acoustics are simulated based on the CFD results. A snapshot of the near fan region is depicted in Figure 4a. The sound waves, originating from the fan inside the duct, propagate into the inlet as well as the outlet chamber. Different qualitative characteristics can be identified for both chambers, which are caused by the sound source distribution. The iso-surfaces in Figure 4a show the source term of the PCWE. More detailed investigations confirm that the dominant sound sources are occurring at the suction side of the fan, spatially concentrated around the leading edges of the fan blades and in the wake of tip gap flow effects hitting the following blade profiles. In agreement with the findings from [1] and [3], these source mechanisms are associated with the BPF and the even more important subharmonics of the BPF. To compare the numerical results for different HAS approaches, time signals of the sound pressure are depicted in Figure 4b. The probe location is placed at the mid-line of the duct inlet area inside the hydrodynamic source region. The comparison of the results shows that the qualitative behavior is nearly identical for all approaches. The two HAS systems APE-2 and LPCE quantify the sound pressure in the same way. This is also true for the two wave equations, namely the PCWE and the wave equation formulation of the LPCE. All time signals in Figure 4b clearly include harmonic components, which can be associated with orders of the BPF or subharmonic parts. Both curve trends, associated to HAS system or wave equation, only partially vary in the form of time dependent amplitude shifts. As these phenomena are observable for the whole simulation time including positive and negative shifts, a unique quantitative statement is not possible yet. Additional investigations via frequency domain transformation of the time signals completely shade these differences and make them unidentifiable. As a consequence of the derivations of the HAS approaches, the numerical results for the present benchmark case only differ in the source region as identified in Figure 4b. Extending the evaluation to the microphone positions inside the anechoic inlet chamber gives the possibility to discuss the acoustic results. Figure 5 shows different PSD results for the microphones 4 and

5 from the experiment [1]. As all HAS approaches give nearly identical results, only the two wave equations and the experimental data are depicted in Figure 5. Comparing the numerical results, the introduced wave equation formulation of the LPCE shows its applicability and consistency by predicting the induced aeroacoustics in agreement with the PCWE. As the same numerical setup and CFD data is used for both simulations, this verifies the approach. The comparison of the numerical results with the measurement data in Figure 5 shows good accordance in the global trend. Blade passing subharmonic tonal components dominate the spectra and the frequency shifts are in common with underlying CFD results (first subharmonic at ≈ 315 Hz instead of 340 Hz). Directly in front of the duct, the numerical results meet the experiment well until the upper mesh frequency of 700 Hz and the BPF itself is invisible (see Figure 5a). Especially for microphone 5, the incorrect flow effects of the first subharmonic from CFD result in over prediction of the amplitudes (see Figure 5b). Comparing the amplitude overshoot in wall pressure (see Figure 3a) with the peak value error at microphone 5, similar deviations are observable. Overall, the acoustic results give a plausible prediction highlighting the need for more precise CFD results as aeroacoustic source fields. Based on the numerical effort for different HAS approaches, the PCWE is preferable for the axial fan benchmark case. As the wave equation formulation of the LPCE includes an additional term (see Eq. (13), term II), the numerical effort in each time step is higher.



(a) Snapshot of p^a , where blue/red refer to small/high values and the source term is visualized on iso-surfaces in green (PCWE). (b) Time signals of the sound pressure at the inlet of the duct.

Figure 4. Spatial and time resolved CAA results for the axial fan.



(a) Microphone 4 directly in front of the duct (distance 1 m, 0°). (b) Microphone 5 in front of the duct (distance 1 m, 30°).

Figure 5. PSD of the pressure $p = p^{ic} + p^a$ at different microphone positions inside the inlet chamber.

Nevertheless, in comparison to the original LPCE, the wave equation formulation has the potential to be much faster generating the same acoustic results. As less equations and only scalar solution variables are necessary, transient flow coupling mechanisms can be included efficiently in sound prediction by Eq. (13).

6 CONCLUSIONS

In the present paper an axial fan benchmark case for aeroacoustics [1] was investigated numerically. Based on transient CFD results, different HAS approaches were applied to compute the induced sound field. The simplified CFD simulation showed acceptable results including the main characteristics of the turbulent flow. Nevertheless, the CAA results emphasized the need for a more detailed CFD model. Finally, all HAS approaches gave consistent results and the introduced wave equation formulation showed promising potential. In the future, a more detailed investigation of the flow is planned to yield an improved numerical prediction of the aeroacoustics. Furthermore, numerical studies of the wave equation formulation of the LPCE are intended.

REFERENCES

- [1] Zenger, F.; Junger, C.; Kaltenbacher, M.; Becker, S. A Benchmark Case for Aerodynamics and Aeroacoustics of a Low Pressure Axial Fan. SAE Technical Paper 2016-01-1805, 2016.
- [2] Moon, Y.-J. Sound of fluids at low Mach numbers. *European Journal of Mechanics B/Fluids*, Vol 40, 2013, pp 50-63.
- [3] Junger, C.; Zenger, F.; Reppenhagen, A.; Kaltenbacher, M.; Becker, S. Numerical Simulation of a Benchmark Case for Aerodynamics and Aeroacoustics of a Low Pressure Axial Fan. *Proceedings of INTER-NOISE 2016*, Hamburg, Germany, 2016.
- [4] Ewert, R.; Schröder, W. Acoustic perturbation equations based on flow decomposition via source filtering. *Journal of Computational Physics*, Vol 188 (2), 2003, pp 365-398.
- [5] Hüppe, A. Spectral finite elements for acoustic field computation. Ph. D. Thesis, University of Klagenfurt, Austria, 2013.
- [6] Seo, J.-H.; Moon, Y.-J. Perturbed Compressible Equations for Aeroacoustic Noise Prediction at Low Mach Numbers. *AIAA Journal*, Vol 43 (8), 2005, pp 1716-1724.
- [7] Seo, J.-H.; Moon, Y.-J. The Linearized Perturbed Compressible Equations for Aeroacoustic Noise Prediction at Very Low Mach Numbers. *AIAA Journal*, Vol 218 (2), 2006, pp 702-719.
- [8] Pierce, A. D. Wave equation for sound in fluids with unsteady inhomogeneous flow. *Journal of the Acoustical Society of America*, Vol 87 (6), 1990, pp 2292-2299.
- [9] Piepiorka, J.; Schröder, T.; Silkeit, P.; von Estorff, O. Weiterentwicklung und Untersuchung eines Strömungsakustik-Lösers für rotierende Gitter in OpenFOAM®. *Proceedings of Fortschritte der Akustik - DAGA 2018*, Munich, Germany, 2018.
- [10] Farrell, P. E.; Maddison, J. R. Conservative interpolation between volume meshes by local Galerkin projection. *Computer Methods in Applied Mechanics and Engineering*, Vol 200 (1-4), 2010, pp 89-100.
- [11] Schröder, T.; von Estorff, O. Influence of Source Term Interpolation on hybrid Computational Aeroacoustics in Finite Volumes. *Proceedings of INTER-NOISE 2016*, Hamburg, Germany, 2016.
- [12] Piepiorka, J.; Kranz, O.; Wurm, F.-H.; von Estorff, O. Numerische Simulation und Untersuchung des Strömungsschalls in einer Radialpumpe. *Proceedings of Fortschritte der Akustik - DAGA 2019*, Rostock, Germany, 2019.